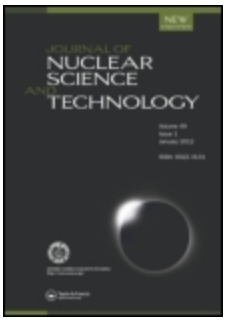

Oxidation behavior of Ce and Gd doped $(U,Zr)O_2$

Journal:	*Journal of Nuclear Science and Technology*
Manuscript ID	TNST-2022-0116
Manuscript Type:	Article
Date Submitted by the Author:	29-May-2022
Complete List of Authors:	Sun, Yifan; Kyoto University Institute for Integrated Radiation and Nuclear Science, Institute for Integrated Radiation and Nuclear Science Watanabe, Shiho; Osaka University School of Engineering Graduate School of Engineering, Division of Sustainable Energy and Environmental Engineering Muta, Hiroaki; Osaka University School of Engineering Graduate School of Engineering, Division of Sustainable Energy and Environmental Engineering Ohishi, Yuji; Osaka University School of Engineering Graduate School of Engineering, Division of Sustainable Energy and Environmental Engineering Kurosaki, Ken; Kyoto University Institute for Integrated Radiation and Nuclear Science, Institute for Integrated Radiation and Nuclear Science
Keywords:	severe accident, fuel debris, (U,Zr)O2, CeO2, Gd2O3, re-critically analysis
Subject Classification:	801 Nuclear Materials(Vessel, Piping, Fuel, Core Structure, Functional) < 8 Nuclear Materials and Nuclear Fuels, 306 Nuclear Criticality Safety < 3 Reactor Physics, 712 Severe Accident < 7 Operational Management of Reactor, Nuclear Safety Engineering, 806 Fundamental Properties of Nuclear Materials and Fuels < 8 Nuclear Materials and Nuclear Fuels

ARTICLE

Typeset with jnst.cls <ver.2.1>

Oxidation behavior of Ce and Gd doped $(U,Zr)O_2$

Yifan Sun[1,2*], Shiho Watanabe[2], Hiroaki Muta[2], Yuji Ohishi[2] and Ken Kurosaki[1,3†]

[1] *Institute for Integrated Radiation and Nuclear Science, Kyoto University, Japan;*

[2] *Graduate School of Engineering, Osaka University, Japan;*

[3] *Research Institute of Nuclear Engineering, University of Fukui, Japan;*

Re-criticality analysis of the fuel debris at the Fukushima Dai-ichi Nuclear Power Plant is the key step to ensure the safe retrieval and storage of the fuel debris. Knowledge on the amount and distribution of Pu and Gd within the fuel debris greatly contributes to such analysis as they directly affect the fission chain-reaction. However, not much is known about how Pu and Gd doped $(U,Zr)O_2$ solid solutions oxidizes and whether a Pu/Gd-concentrated phase will form. In this study, CeO_2 was used as a surrogate material for PuO_2. We fabricated $(U,Zr,Ce)O_2$ and $(U,Zr,Gd)O_2$ solid solutions and heated these samples in air at 1073 K for two hours. Samples doped with 5 mol% Ce and Gd only showed a single orthorhombic-U_3O_8 phase after oxidation, and the XRD peak intensity of the orthorhombic phase decreased with the amount of dopant added. For $(U,Zr,Gd)O_2$, its phase transformation with further oxidation is found to be cubic-$(U,Zr,Gd)_4O_9$ → orthorhombic-$(U,Zr,Gd)_3O_7$ → orthorhombic-$(U,Zr,Gd)_3O_8$. Based on SEM/EDS images, we concluded that Ce (Pu's surrogate) and Gd are uniformly distributed in the $(U,Zr,RE)O_2$ (RE=Ce, Gd) samples after oxidation.

Keywords: Severe accident; Fuel debris; $(U,Zr)O_2$; CeO_2; Gd_2O_3; Re-critically analysis

J. Nucl. Sci. & Technol. Article

1. Introduction

On March 11th, 2011, the Tsunami following the Tohoku earthquake led to a power loss at the Fukushima Dai-ichi Nuclear Power Plant (1F), causing Units 1-3's reactor pressure vessels (RPV) to overheat due to the loss of coolants. As temperature elevates, UO_2 fuel pellets, Zircolay fuel claddings, control materials, as well as other metallic components melted, penetrated the bottom of the RPV, and reacted with the concrete pedestal supporting the RPV[1, 2]. The retrieval of these solidified fuel debris is an important step for decommissioning 1F.

Before debris retrieval takes place, it is necessary to understand the composition and thermophysical/mechanical properties of the fuel debris. Studies from the TMI-2 accident[3, 4] and molten core concrete interaction (MCCI) simulations[5, 6] found that (U,Zr)O_2 solid solution is the major oxide component of the fuel debris. The physical properties of the (U,Zr)O_2 solid solution, various Fe/Zr containing alloys, and MCCI products have been clarified in recent years[7–18]. On the other hand, re-criticality due to the presence of Pu/Gd and the sudden fragmentation or relocation of the fuel debris during retrieval is a major concern during decommissioning[19, 20]. Pu and Gd are two of the crucial elements within the 1F fuel debris that affects the fission chain reaction. Pu isotopes are formed from U^{238} neutron captures, and Gd is added to nuclear fuels as a burnable poison because of its large neutron absorption cross-section. Because the 1F fuel debris could become oxidized from water radiolysis[21–23], it is necessary to clarify the oxidation behavior of fuel debris for re-criticality analysis.

The oxidation of UO_2 and rare earth elements (REs) doped-UO_2 has been extensively investigated for the safe handling and storage of nuclear fuels. At low temperatures, UO_2 oxidizes to U_3O_8 in two steps: $UO_2 \rightarrow U_4O_9/U_3O_7 \rightarrow U_3O_8$[24, 25]. $U_3O_7 \rightarrow U_3O_8$ is observed in the oxidation of non-irradiated UO_2 or slightly doped-UO_2[26, 27], while

*Corresponding author. Email: sun.yifan.7r@kyoto-u.ac.jp

†Corresponding author. Email: kurosaki.ken.6n@kyoto-u.ac.jp

$U_4O_9 \rightarrow U_3O_8$ is found in spent nuclear fuel during oxidation[28]. Structural and thermal analysis studies have found that adding dopants such as Pu[29,30], La[31,32], Nd[33,34], Ce[34–37], Gd[28,38–40], or Zr[41] can hinder the oxidation of UO_2 into U_3O_8 by keeping the cubic fluorite structure stable at higher temperatures, and this oxidation resistance increases with increasing dopant amount. However, it is unclear how the oxidation of UO_2 proceeds with multiple dopants, as in the case of the fuel debris. For fuel debris re-criticality analysis, we still lack information on the phase states and element distribution of Pu or Gd doped-(U,Zr)O_2 after oxidation.

Therefore, in this work, we focused on investigating the oxidation behavior of Pu and Gd doped-(U,Zr)O_2 to fill the gap in the existing literature. CeO_2 is used in this study as a surrogate material for PuO_2 because of the similarities in their crystal structures[42,43]. (U,Zr,Ce)O_2 and (U,Zr,Gd)O_2 samples were prepared using spark plasma sintering (SPS) and heated in air. The phase states of the oxidized samples, which allows us to understand the sample's oxidation pathways, were characterized using X-ray diffraction (XRD). The distribution of Ce and Gd in oxidized-(U,Zr,Ce/Gd)O_2 is observed with scanning electron microscopy/energy dispersive spectroscopy (SEM/EDS).

2. Experimental Methods

2.1. Sample Preparation

To evaluate the distribution of Ce and Gd within (U,Zr)O_2 after oxidation, we fabricated $(U_{0.9-x}Zr_{0.1}RE_x)O_2$ (RE=Ce, Gd) (x=0, 0.05) solid solution samples. 10 mol% ZrO_2 was selected based on its solubility in UO_2 at 1773 K, as shown in the UO_2-ZrO_2 phase diagram in Fig.1. Generally, around 1 at% Pu is found in spent nuclear fuel[44], and the amount increases with increasing burn-up or if mixed oxide (MOX) fuel is used instead[45]. The amount of Gd_2O_3 burnable poison added to UO_2 is generally less than 8 wt%[28,46], but additional $(U_{0.9-x}Zr_{0.1}Gd_x)O_2$ (x=0.1, 0.15, 0.2, 0.25) samples were pre-

pared to investigate the effect of the amount of doped Gd on the phases formed after oxidation.

[Figure 1 about here.]

Stoichiometric amount of UO_2, ZrO_2 (4N, Furuuchi Chemical), CeO_2 (4N, Furuuchi Chemical), and Gd_2O_3 (3N, Furuuchi Chemical) powders were first mixed and cold-pressed at a pressure of 200 MPa and held for 10 minutes. The prepared green pellets were then sintered in an argon atmosphere for 10 hours at 1773 K. Finally, to oxidize the (U, Zr, RE)O_2 samples, we heated them at 1073 K for 2 hours in air.

2.2. Characterization methods

To clarify the phase states of the sintered and oxidized samples, we performed XRD from $2\theta = 20^o$ to 90^o (CuKα radiation, Rigaku Ultima-IV). The lattice parameters were calculated using the least squares method. SEM/EDS analysis (JSM-6500F, JEOL) was then conducted to investigate the element distribution within the fabricated samples.

3. Results and Discussion

3.1. Effect of Ce doping on $(U_{0.9}Zr_{0.1})O_2$

3.1.1. Sintered $(U_{0.9-x}Zr_{0.1}Ce_x)O_2$ (x=0, 0.05)

The XRD patterns of the sintered (U,Zr,Ce)O_2 samples are shown in Fig. 2, and the cubic phase's lattice parameters are shown in Table 1. Only cubic structure peaks were observed in the XRD patterns, suggesting that (U,Zr,Ce)O_2 solid solution samples were successfully fabricated. The SEM/EDS images of the sintered samples in Fig. 3 also show that the constituent elements are uniformly distributed.

[Figure 2 about here.]

[Table 1 about here.]

[Figure 3 about here.]

Although there are no previous reports on (U,Zr,Ce)O_2, the published lattice parameters of Zr doped UO_2 are larger than the one reported in this study. For example, both Kulkarni et al.[41] and Sali et al.[47] reported a lattice parameter of 0.5440 nm for $(U_{0.9}Zr_{0.1})O_2$ sintered under a slightly reducing atmosphere (Ar+8%H_2). In the same studies[41, 47], it was shown that sintering with pure commercial argon gas is not enough to prevent the oxidation of cubic-(U,Zr)O_2 into cubic-(U,Zr)O_{2+x}, which results in a smaller lattice parameter as shown in Table.2. This reduction is expected because the cubic-UO_{2+x} lattice has been shown to contract as uranium is oxidized[48–50]. This suggests that the (U,Zr,Ce)O_2 and (U,Zr,Gd)O_2 samples prepared under argon atmosphere in this work should be hyperstoichiometric oxides (U,Zr,RE)O_{2+x}.

As mentioned in the introduction, the purpose of the current study is not to report the structure of doped stoichiometric uranium dioxides but to investigate the distribution of Ce and Gd within the fuel debris after oxidization. In this case, hyperstoichiometric starting materials do not affect the outcome of the experiment because we are interested in the final oxidized products. For simplicity, the sintered samples are referred to as $(U_{0.9-x}Zr_{0.1}RE_x)O_2$, and the samples after oxidation in air are referred to as oxidized $(U_{0.9-x}Zr_{0.1}RE_x)O_2$ in this study.

[Table 2 about here.]

3.1.2. Oxidized $(U_{0.9-x}Zr_{0.1}Ce_x)O_2$ (x=0, 0.05)

From the XRD patterns shown in Fig. 4, we can see that $(U_{0.9}Zr_{0.1})O_2$ transforms from cubic-$(U_{0.9}Zr_{0.1})O_2$ to orthorhombic-$(U_{0.9}Zr_{0.1})_3O_8$ upon oxidation. The lattice parameters of the orthorhombic phases are calculated and listed in Table 3. This phase transformation of $(U_{0.9}Zr_{0.1})O_2$ accompanying oxidation is consistent with the results from the thermogravimetric study done by Kulkarni et al.[41], which showed that the solubility of Zr in orthorhombic-U_3O_8 at 1073 K to be around 20 mol%. Above the solubility limit, a

mixture of tetragonal-ZrO_2 and orthorhombic-$(U,Zr)_3O_8$ is obtained after oxidation[41].

[Figure 4 about here.]

[Table 3 about here.]

For Ce-doped UO_2, Olds et al.[34] found that the formation of the orthorhombic-U_3O_8 phase was delayed by roughly 50 K with the addition of 5 mol% CeO_2. Although its formation is retarded, orthorhombic-U_3O_8 still becomes the dominant phase, and the cubic phase eventually disappears in oxidized $(U,Ce)O_2$ samples with increasing temperature[34, 37]. Similarly, for $(U_{0.85}Zr_{0.1}Ce_{0.05})O_2$, the added 5 mol% CeO_2 did not prevent $(U_{0.85}Zr_{0.1}Ce_{0.05})O_2$ from completely oxidizing into orthorhombic-$(U_{0.85}Zr_{0.1}Ce_{0.05})_3O_8$ when heated at 1073 K. Furthermore, from the SEM/EDS images in Fig. 5, we can see that U, Zr, and Ce are uniformly distributed within the oxidized samples. Brett & Fox[52] have reported that the solubility of Pu in U_3O_8 is 10 mol% at 1023 K. Therefore, based on our results for $(U,Zr,Ce)O_2$, we can extrapolate that cubic-$(U_{0.85}Zr_{0.1}Pu_{0.05})O_2$ will most likely transform into single-phase orthorhombic-$(U_{0.85}Zr_{0.1}Pu_{0.05})_3O_8$ when oxidized at 1073 K, with Pu evenly distributed.

[Figure 5 about here.]

3.2. Effect of Gd doping on $(U_{0.9}Zr_{0.1})O_2$

3.2.1. Sintered $(U_{0.9-x}Zr_{0.1}Gd_x)O_2$ (x=0.05 to 0.25)

The XRD patterns and the SEM/EDS images of the sintered $(U_{0.9-x}Zr_{0.1}Gd_x)O_2$ (x=0.05 to 0.25) are shown in Figs.6-7. Although Zr-rich regions can be observed in the EDS images of samples $(U_{0.75}Zr_{0.1}Gd_{0.15})O_2$ and $(U_{0.65}Zr_{0.1}Gd_{0.25})O_2$, only a single cubic phase was detected in the corresponding XRD patterns. Therefore, the fabricated samples are considered as overall homogeneous single-phase cubic-$(U,Zr,Gd)O_2$ solid solutions. It has been shown that the addition of Gd to UO_2 or the formation of oxygen vacancies results in a variation in the cubic phase's lattice parameter[53–55]. No definite

pattern can be found in the lattice parameters of the sintered (U,Zr,Gd)O_2 samples listed in Table 4 because these samples were fabricated under a pure argon atmosphere and are likely to be hyperstoichimetric, as mentioned in section.3.1.1..

[Figure 6 about here.]

[Table 4 about here.]

[Figure 7 about here.]

3.2.2. Oxidized ($U_{0.9-x}Zr_{0.1}Gd_x)O_2$ (x=0.05 to 0.25)

The XRD patterns and the calculated lattice parameters of the oxidized ($U_{0.9-x}Zr_{0.1}Gd_x)O_2$ samples are shown in Fig. 8 and Table 5. By comparing Table 4 and 5, we can see that the cubic phase's lattice parameter decreased after oxidation at each Gd concentration, which is expected considering the cubic-UO_{2+x} lattice contracts upon oxidation[48–50]. Again, Zr-rich regions were observed in the EDS images of ($U_{0.75}Zr_{0.1}Gd_{0.15})O_2$ and ($U_{0.65}Zr_{0.1}Gd_{0.25})O_2$ but not detected in the XRD measurements. Since the solubility of Zr in UO_2 is close to negligible at 1073 K[57], the temperature of the oxidation experiments, it is reasonable that Zr-rich regions still remain after heating in air.

To understand the phases present in the oxidized (U,Zr,Gd)O_2 samples, we first take a look at the oxidation pathway of UO_2 in air, which has been shown to be a two-step process of $UO_2 \rightarrow U_4O_9/U_3O_7 \rightarrow U_3O_8$[24, 25, 35, 39]. Experimental studies using thermogravimetric analysis (TGA) and differential scanning calorimetry (DSC) have shown that doping UO_2 with Gd^{3+} enhances its oxidation resistance[39, 40] and slows down the oxidation kinetics in both steps. Kim et al.[39] reasoned from a charge balance point of view that this retardation is caused by the reduction in the amount of U^{4+} that can be oxidized with increasing Gd^{3+}. Recently, results from density-functional theory (DFT) studies by Hong et al.[58] showed that Gd-doped UO_2's oxidation resistance is the com-

bined effect of reduced active oxygen adsorption energy, adsorption sites, and driving force for subsurface oxygen diffusion.

[Figure 8 about here.]

[Table 5 about here.]

With the knowledge that Gd doping in UO_2 decelerates its oxidation, we can expect the orthorhombic-$(U,Zr,Gd)_3O_8$ diffraction peak's intensity to decrease and the appearance of cubic-$(U,Zr,Gd)_4O_9$ peaks with increasing Gd, which agrees with the XRD patterns shown in Fig. 8. 5 mol% Gd was unable to prevent the $(U_{0.85}Zr_{0.1}Gd_{0.05})O_2$ sample from fully oxidizing into orthorhombic-$(U_{0.85}Zr_{0.1}Gd_{0.05})_3O_8$. Starting from 10 mol% Gd, the cubic phase can be observed in the oxidized sample as Gd noticeably hindered the formation of $(U,Zr,Gd)_3O_8$. Similar behavior was observed for Gd doped UO_2 by Kim et al.[39]. However, for $(U_{0.75}Zr_{0.1}Gd_{0.15})O_2$ and $(U_{0.70}Zr_{0.1}Gd_{0.2})O_2$, the orthorhombic-$(U,Zr,Gd)_3O_8$ phase is replaced with the less oxygen-rich orthorhombic-$(U,Zr,Gd)_3O_7$ (Cmcm, 63), which has not been previously observed in oxidized $(U,Gd)O_2$ solid solutions[38, 39]. The formation of an orthorhombic-$(U,Zr)_3O_7$ phase was originally reported after heating $(U_{0.7}Zr_{0.3})O_2$ in air up to 873 K by Sali et al.[47], who suggested its formation is the result of an excess amount of anions in the cubic-U_4O_9 lattice. Simply put, the orthorhombic-$(U,Zr,Gd)_3O_7$ structure results from a distorted cubic-$(U,Zr,Gd)_4O_9$ lattice. By comparing the lattice parameters of the cubic-$(U,Zr,Gd)_4O_9$ and the orthorhombic-$(U,Zr,Gd)_3O_7$ phases in Table 5, we can notice they indeed resemble each other.

Based on the phases present in the oxidized $(U,Zr,Gd)O_2$ samples, we conclude that the phase transformation as cubic-$(U,Zr,Gd)O_2$ oxides is as follows: cubic-$(U,Zr,Gd)O_2$ $\rightarrow$ cubic-$(U,Zr,Gd)_4O_9$ $\rightarrow$ orthorhombic-$(U,Zr,Gd)_3O_7$ $\rightarrow$ orthorhombic-$(U,Zr,Gd)_3O_8$. With increasing Gd concentration, the proportion of the cubic-$(U,Zr,Gd)_4O_9$ phase formed after oxidation increases, while orthorhombic-$(U,Zr,Gd)_3O_8$ is gradually replaced with the less oxygen-rich orthorhombic-$(U,Zr,Gd)_3O_7$. Furthermore, Gd is a neutron absorber, and

knowledge of its distribution in 1F's fuel debris is essential from the point of re-criticality analysis. From the SEM/EDS results shown in Fig. 9, we can confirm that Gd is uniformly distributed within the oxidized (U,Zr,Gd)O_2 samples and not concentrated in either of the phases.

[Figure 9 about here.]

4. Conclusion

To ensure decommissioning proceeds safely at 1F, we need information on the phase states and distribution of Pu and Gd in the oxidized fuel debris for re-criticality analysis. In this work, single-phase Ce and Gd doped (U,Zr,RE)O_{2+x} solid solution were heated in air at 1073 K for two hours to clarify their oxidation behaviors.

The substitution of U with 5 mol% Ce or Gd in $(U_{0.9}Zr_{0.1})O_2$ was unable to prevent to the sample from transforming completely into orthorhombic-(U,Zr,Ce/Gd)$_3O_8$. As the amount of doped-Gd increases, (U,Zr,Gd)O_2 sample's oxidation, especially the formation of (U,Zr,Gd)$_3O_8$, was inhibited. For $(U_{0.75}Zr_{0.1}Gd_{0.15})O_2$ and $(U_{0.70}Zr_{0.1}Gd_{0.2})O_2$, a less oxygen-rich orthorhombic-(U,Zr,Gd)$_3O_7$ phase was formed along with cubic-(U,Zr,Gd)$_4O_9$ after oxidation. Ce (Pu's surrogate) and Gd (neutron absorber) are found to be evenly distributed after oxidation, suggesting re-criticality analysis should be performed on the oxidized fuel debris as a whole as there are no phases especially concentrated with Pu or Gd.

Disclosure statement

No potential conflict of interest was reported by the authors.

Data availability

The data that support the findings of this study are available from the corresponding authors upon reasonable request.

References

[1] The Fukushima Daiichi Accident, Tech. rep., International Atomic Energy Agency, Vienna, Austria (2015).

[2] N. Akiyama, H. Sato, K. Naito, Y. Naoi, T. Katsuta, Subsidy for decommissioning and contaminated water countermeasures project (improvement of comprehensive core status monitoring) [廃炉・汚染水対策事業費本補助金(総合的な炉内状況把握の高度化)], Tech. rep., International Research Institute for Nuclear Decommissioning (Jun. 2018).

[3] R. K. McCardell, M. L. Russell, D. W. Akers, C. S. Olsen, Summary of TMI-2 core sample examinations, Nucl. Eng. Des. 118 (3) (1990) 441–449.

[4] D. Akers, S. Jensen, B. Schuetz, Examination of relocated fuel debris adjacent to the lower head of the TMI-2 reactor vessel, Tech. rep., Nuclear Regulatory Commission, Washington, DC (United States). (1994).

[5] T. Kitagaki, H. Ikeuchi, K. Yano, H. Ogino, Characterization of the VULCANO test products for fuel debris removal from the Fukushima Daiichi Nuclear Power Plant, Prog. Nucl. Sci. Technol. (2018).

[6] T. Kitagaki, K. Yano, H. Ogino, T. Washiya, Thermodynamic evaluation of the solidification phase of molten core–concrete under estimated Fukushima Daiichi Nuclear Power Plant accident conditions, J. Nucl. Mater. 486 (2017) 206–215.

[7] F. Nakamori, Y. Ohishi, M. Kumagai, H. Muta, K. Kurosaki, K. Fukumoto, S. Yamanaka, Mechanical and Thermal Properties of Fe_2B, Trans. At. Energy Soc. Japan 15 (4) (2016) 223–228.

[8] D. Okada, H. Ishii, Y. Ohishi, H. Muta, K. Kurosaki, Thermal and Mechanical Properties of Fe_2Zr, Trans. At. Energy Soc. Japan 18 (1) (2019) 37–42.

[9] Y. Sun, Y. Abe, H. Muta, Y. Ohishi, Mechanical and thermal properties of Zr-B and Fe-B alloys, J. Nucl. Sci. Technol. 57 (8) (2020) 917–925.

[10] Y. Ohishi, M. Sugizaki, Y. Sun, H. Muta, K. Kurosaki, Thermophysical and mechanical properties of CrB and FeB, J. Nucl. Sci. Technol. 56 (9-10) (2019) 859–865.

[11] F. Nakamori, Y. Ohishi, H. Muta, K. Kurosaki, K. Fukumoto, S. Yamanaka, Mechanical and thermal properties of bulk ZrB_2, J. Nucl. Mater. 467 (2015) 612–617.

[12] F. Nakamori, Y. Ohishi, H. Muta, K. Kurosaki, K. Fukumoto, S. Yamanaka, Mechanical and thermal properties of $ZrSiO_4$, J. Nucl. Sci. Technol. 54 (11) (2017) 1267–1273.

[13] Y. Ohishi, Y. Sun, Y. Ooi, H. Muta, Mechanical properties and thermal conductivity of (U,Zr)SiO_4, J. Nucl. Mater. 556 (2021) 153160.

[14] T. Kitagaki, H. Ikeuchi, K. Yano, L. Brissonneau, B. Tormos, R. Domenger, J. Roger, T. Washiya, Effect of quenching on molten core-concrete interaction product, J. Nucl. Sci. Technol. 56 (9-10) (2019) 902–914.

[15] C. H. Zheng, H. P. Wang, P. F. Zou, L. Hu, B. Wei, Determining thermophysical properties of normal and metastable liquid Zr-Fe alloys by electrostatic levitation method, Metall. Mater. Trans. A 51 (2020) 4074–4085.

[16] A. Seibert, D. Staicu, D. Bottomley, M. Cologna, J. Boshoven, H. Hein, E. Kassim, S. N. M. Ernstberger, D. Robba, R. Konings, Thermophysical properties of U, Zr-oxides as prototypic corium materials, J. Nucl. Mater. 520 (2019) 165–177.

[17] Y. Ohishi, K. Kurokawa, Y. Sun, H. Muta, Thermophysical properties of molten $Zr_{1-x}O_x$ (x=0.1, 0.2) measured by electrostatic levitation, J. Nucl. Mater. 528 (2020) 151873.

[18] Y. Ohishi, H. Muta, K. Kurosaki, J. T. Okada, T. Ishikawa, Y. Watanabe, S. Yamanaka, Thermophysical properties of molten core materials: Zr–Fe alloys measured by electrostatic levitation, J. Nucl. Sci. Technol. 53 (12) (2016) 1943–1950.

[19] K. Nakajima, Issue on Criticality Safety Control of Fuel Debris - Preparation for the Decommissioning of Reactors at the Fukushima Daiichi Nuclear Power Plant, J. At. Energy Soc. Japan 56 (4)

(2014) 230–234.

[20] I. R. I. for Nuclear Decommissioning, Development of analysis and estimation technologies for fuel debris characterization, results for FY2019 (9 2020).

[21] A. Kirishima, M. Hirano, T. Sasaki, N. Sato, Leaching of actinide elements from simulated fuel debris into seawater, J. Nucl. Sci. Technol. 52 (10) (2015) 1240–1246.

[22] B. Grambow, A. Nitta, A. Shibata, Y. Koma, S. Utsunomiya, R. Takami, K. Fueda, T. Ohnuki, C. Jegou, H. Laffolley, et al., Ten years after the NPP accident at Fukushima: review on fuel debris behavior in contact with water, J. Nucl. Sci. Technol. 59 (1) (2022) 1–24.

[23] P. C. Burns, R. C. Ewing, A. Navrotsky, Nuclear fuel in a reactor accident, Science 335 (6073) (2012) 1184–1188.

[24] J. Belle, Uranium dioxide: properties and nuclear applications, Vol. 4, Naval Reactors, Division of Reactor Development, US Atomic Energy Commission, 1961.

[25] R. J. McEachern, P. Taylor, A review of the oxidation of uranium dioxide at temperatures below 400C, J. Nucl. Mater. 254 (2-3) (1998) 87–121.

[26] P. Taylor, E. A. Burgess, D. G. Owen, An x-ray diffraction study of the formation of β-uo2. 33 on uo2 pellet surfaces in air at 229 to 275° c, J. Nucl. Mater. 88 (1) (1980) 153–160.

[27] S. R. Teixeira, K. Imakuma, High temperature x-ray diffraction study of the u4o9 formation on uo2 sintered plates, J. Nucl. Mater. 178 (1) (1991) 33–39.

[28] L. Thomas, R. Einziger, H. Buchanan, Effect of fission products on air-oxidation of LWR spent fuel, J. Nucl. Mater. 201 (1993) 310–319.

[29] V. Tennery, T. Godfrey, Oxidation properties of (u, pu) o2 solid solutions, J. Am. Ceram. Soc. 56 (3) (1973) 129–133.

[30] J. Rouault, J. Girardin, Heatings of untight lmfbr fuel elements under oxidising atmospheres: French experience review, in: Proceedings of a Workshop on Chemical Reactivity of Oxide Fuel and Fission Product Release. Ed. KA Simpson and P. Wood (Berkeley, UK, CEGB, 1987), 1987, pp. 245–260.

[31] Z. Talip, T. Wiss, P. E. Raison, J. Paillier, D. Manara, J. Somers, R. J. Konings, Raman and X-ray

studies of uranium–lanthanum-mixed oxides before and after air oxidation, J. Am. Ceram. Soc. 98 (7) (2015) 2278–2285.

[32] W. Wilson, C. Alexander, A. Gerds, Stabilization of uo2, J. Inorg. Nucl. 20 (3-4) (1961) 242–251.

[33] R. McEachern, D. Doern, D. Wood, The effect of rare-earth fission products on the rate of U_3O_8 formation on UO_2, J. Nucl. Mater. 252 (1) (1998) 145–149.

[34] T. A. Olds, S. E. Karcher, K. W. Kriegsman, X. Guo, J. S. McCloy, Oxidation and anion lattice defect signatures of hypostoichiometric lanthanide-doped UO_2, J. Nucl. Mater. 530 (2020) 151959.

[35] Y.-K. Ha, J. Lee, J.-G. Kim, J.-Y. Kim, Effect of Ce doping on UO_2 structure and its oxidation behavior, J. Nucl. Mater. 480 (2016) 429–435.

[36] S. K. Sali, M. Keskar, R. Phatak, K. Krishnan, G. P. Shelke, P. P. Muhammed Shafeeq, S. Kannan, Oxidation behavior of $(U_{1-y}Ce_y)O_{2.00}$; (y = 0.21, 0.28 and 0.44) solid solutions under different oxygen potentials. Thermogravimetric and in situ X-ray diffraction studies, J. Nucl. Mater. 510 (2018) 499–512.

[37] H. Nawada, P. Sriramamurti, K. Kutty, S. Rajagopalan, R. Yadav, P. Rao, C. Mathews, Oxidation and phase behaviour studies of the U-Ce-O system, J. Nucl. Mater. 139 (1) (1986) 19–26.

[38] Y.-K. Ha, J.-G. Kim, Y.-J. Park, W.-H. Kim, Studies on the air-oxidation behavior of uranium dioxide I. Phase transformation from $(U_{1-y}Gd_y)O_2$ to $(U_{1-y}Gd_y)_3O_8$, J. Nucl. Sci. Technol. 39 (2002) 772–775.

[39] J.-G. Kim, Y.-K. Ha, S.-D. Park, K.-Y. Jee, W.-H. Kim, Effect of a trivalent dopant, Gd^{3+}, on the oxidation of uranium dioxide, J. Nucl. Mater. 297 (3) (2001) 327–331.

[40] R. D. Scheele, B. D. Hanson, A. M. Casella, Effect of added gadolinium oxide on the thermal air oxidation of uranium dioxide, J. Nucl. Mater. 552 (2021) 153008.

[41] N. Kulkarni, K. Krishnan, U. Kasar, S. Rakshit, S. Sali, S. Aggarwal, Thermal studies on fluorite type $Zr_yU_{1-y}O_2$ solid solutions, J. Nucl. Mater. 384 (2) (2009) 81–86.

[42] R. Vauchy, P. Fouquet-Métivier, P. M. Martin, C. Maillard, I. Solinhac, C. Guéneau, C. Léorier, New sample stage for characterizing radioactive materials by X-ray powder diffraction: application

on five actinide dioxides ThO_2, UO_2, NpO_2, PuO_2 and AmO_2, J. Appl. Crystallogr. 54 (2) (2021) 636–643.

[43] J. D. McCullough, An X-ray study of the rare-earth oxide systems: Ce^{IV}—Nd^{III}, Cr^{IV}—Pr^{III}, Ce^{IV}—Pr^{IV} and Pr^{IV}—Nd^{III}, J. Am. Chem. Soc. 72 (3) (1950) 1386–1390.

[44] R. C. Ewing, Long-term storage of spent nuclear fuel, Nat. Mater. 14 (3) (2015) 252–257.

[45] Y. Ando, H. Takano, Estimation of lwr spent fuel composition (1999).

[46] Characteristics and use of urania-gadolinia fuels, Tech. rep., INTERNATIONAL ATOMIC ENERGY AGENCY, Vienna, Austria (1995).

[47] S. Sali, N. Kulkarni, K. Krishnan, S. Achary, A. Tyagi, Oxidation/reduction studies on $Zr_yU_{1-y}O_{2+x}$ and delineation of a new orthorhombic phase in U–Zr–O system, J. Solid State Chem. 181 (8) (2008) 1859–1866.

[48] V. A. Alekseyev, L. A. Anan'yeva, R. P. Rafal'skiy, Effects of composition on lattice parameter of UO_{2+x}, Int. Geol. Rev. 23 (10) (1981) 1229–1236.

[49] J. M. Elorrieta, L. J. Bonales, N. Rodríguez-Villagra, V. G. Baonza, J. Cobos, A detailed Raman and X-ray study of UO_{2+x} oxides and related structure transitions, Phys. Chem. Chem. Phys. 18 (2016) 28209–28216.

[50] F. Bruneval, M. Freyss, J.-P. Crocombette, Lattice constant in nonstoichiometric uranium dioxide from first principles, Phys. Rev. Materials 2 (2018) 023801.

[51] R. Ackermann, A. Chang, C. A. Sorrell, Thermal expansion and phase transformations of the U_3O_{8-z} phase in air, J. Inorg. Nucl. Chem. 39 (1) (1977) 75–85.

[52] N. Brett, A. Fox, Oxidation products of plutonium dioxide-uranium dioxide solid solutions in air at 750 c, J. Inorg. Nucl. 28 (5) (1966) 1191–1203.

[53] R. V. Krishnan, G. Panneerselvam, P. Manikandan, A. MP, K. Nagarajan, Heat capacity and thermal expansion of uranium-gadolinium mixed oxides, J. Nucl. Radiochem. Sci. 10 (1) (2009) 119–126.

[54] T. Ohmichi, S. Fukushima, A. Maeda, H. Watanabe, On the relation between lattice parameter and O/M ratio for uranium dioxide-trivalent rare earth oxide solid solution, J. Nucl. Mater. 102 (1-2)

(1981) 40–46.

[55] N. Liu, J. Kim, J. Lee, Y.-S. Youn, J.-G. Kim, J.-Y. Kim, J. J. Noël, D. W. Shoesmith, Influence of Gd doping on the structure and electrochemical behavior of UO_2, Electrochim. Acta 247 (2017) 496–504.

[56] X. Zhang, Dept. of Earth and Environmental Sciences, Univ. of Michigan, Ann Arbor, MI, USA. Private Communication (2016).

[57] R.G.J.Ball, M.A.Mignanelli, T.I.Barry, J.A.Gisby, The calculation of phase equilibria of oxide core-concrete systems, J. Nucl. Mater. 201 (1993) 238–249.

[58] M. Hong, H. Chun, C. Kwon, B. Han, Outstanding stability of Gd-doped UO_2 against surface oxidation: First-principles study, Appl. Surf. Sci. 589 (2022) 152955.

Table 1 Lattice parameters of the (U,Zr,Ce)O_2 samples sintered under Ar

Sample	Lattice parameter, nm
$(U_{0.9}Zr_{0.1})O_2$	0.5406
$(U_{0.85}Zr_{0.1}Ce_{0.05})O_2$	0.5418

Table 2 Lattice parameters of $(U_{0.9}Zr_{0.1})O_2$ samples sintered under different conditions

Sample	Lattice parameter, nm	Comments
$(U_{0.9}Zr_{0.1})O_2$	0.5440	1673 K, Ar/8%H_2[47]
	0.5440	1673 K, Ar then Ar/8%H_2[41]
	0.5406	This study
$(U_{0.9}Zr_{0.1})O_{2+x}$	0.5385	1673 K, Ar[47]
	0.5385	1673 K, Ar[41]
	0.5405	773 K, air[41]

Table 3 Lattice parameters of the oxidized (U,Zr,Ce)O_2 samples

Sample	Lattice parameters, nm		
	a	b	c
Oxidized $(U_{0.9}Zr_{0.1})O_2$	0.679	1.1704	0.4131
Oxidized $(U_{0.85}Zr_{0.1}Ce_{0.05})O_2$	0.667	1.1717	0.4135

Table 4 Lattice parameters of the $(U_{1-x}Zr_{0.1}Gd_x)O_2$ samples sintered under Ar

Sample	Lattice parameter, nm
$(U_{0.85}Zr_{0.1}Gd_{0.05})O_2$	0.5414
$(U_{0.80}Zr_{0.1}Gd_{0.1})O_2$	0.5411
$(U_{0.75}Zr_{0.1}Gd_{0.15})O_2$	0.5410
$(U_{0.70}Zr_{0.1}Gd_{0.2})O_2$	0.5416
$(U_{0.65}Zr_{0.1}Gd_{0.25})O_2$	0.5411

Table 5 Lattice parameters of the oxidized $(U_{1-x}Zr_{0.1}Gd_x)O_2$ samples

Sample	Cubic, (nm)	Orthorhombic, (nm)			Orthorhombic
	a	a	b	c	space group
Oxidized $(U_{0.85}Zr_{0.1}Gd_{0.05})O_2$	-	0.656	1.174	0.4139	Cmmm, 65
Oxidized $(U_{0.80}Zr_{0.1}Gd_{0.1})O_2$	0.5403	0.664	1.190	0.4131	Cmmm, 65
Oxidized $(U_{0.75}Zr_{0.1}Gd_{0.15})O_2$	0.5402	0.523	0.5479	0.561	Cmcm, 63
Oxidized $(U_{0.70}Zr_{0.1}Gd_{0.2})O_2$	0.5403	0.521	0.551	0.553	Cmcm, 63
Oxidized $(U_{0.65}Zr_{0.1}Gd_{0.25})O_2$	0.5410		-		-

Figure Captions

Figure 1 UO_2-ZrO_2 phase diagram[57]

Figure 2 XRD patterns of the (U,Zr,Ce)O_2 samples sintered under Ar with reference[56]

Figure 3 SEM/EDS images of the (U,Zr,Ce)O_2 samples sintered under Ar.

Figure 4 XRD patterns of the oxidized (U,Zr,Ce)O_2 samples with reference[51].

Figure 5 SEM/EDS images of the oxidized (U,Zr,Ce)O_2 samples

Figure 6 XRD patterns of the $(U_{1-x}Zr_{0.1}Gd_x)O_2$ samples sintered under Ar with reference[56]

Figure 7 SEM/EDS images of the $(U_{1-x}Zr_{0.1}Gd_x)O_2$ samples sintered under Ar.

Figure 8 XRD patterns of the oxidized $(U_{1-x}Zr_{0.1}Gd_x)O_2$ samples with references[47, 51, 56].

Figure 9 SEM/EDS images of the oxidized (U,Zr,Gd)O_2 samples

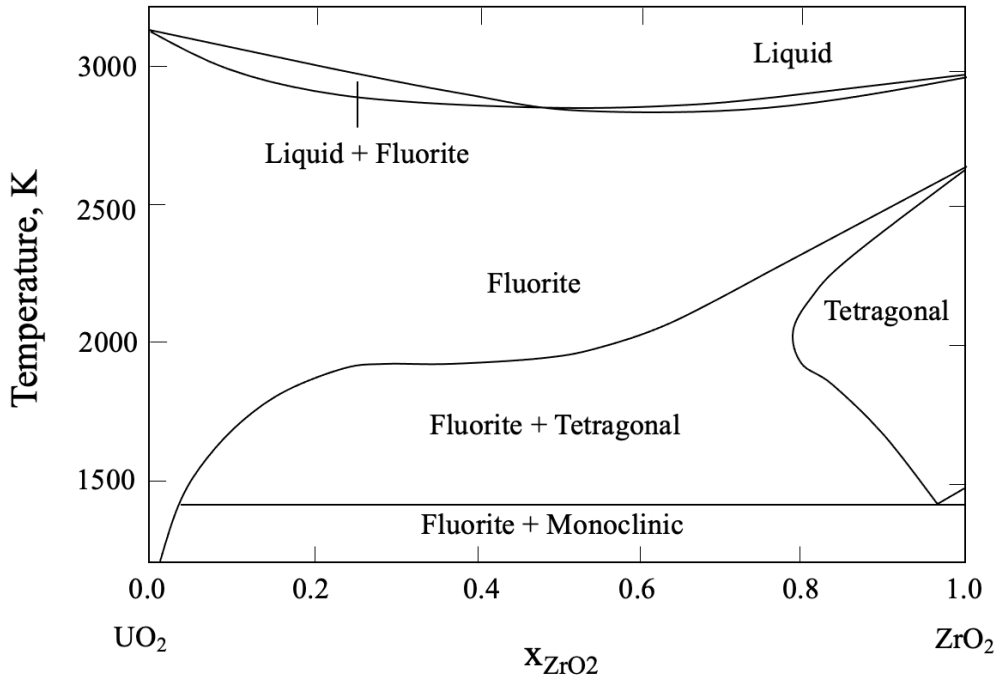

Figure 1 UO_2-ZrO_2 phase diagram[57]

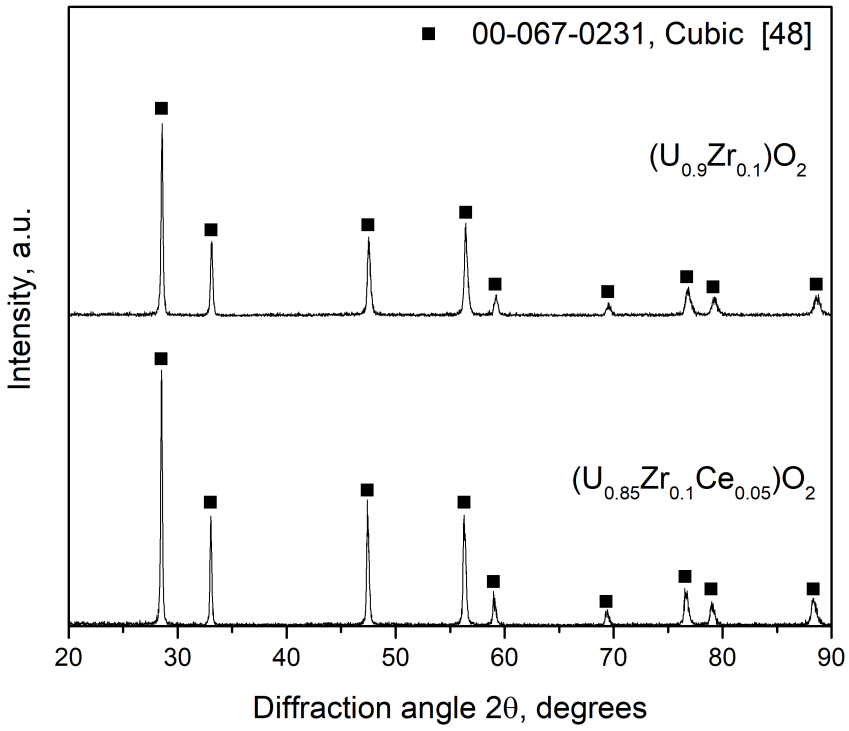

Figure 2 XRD patterns of the (U,Zr,Ce)O_2 samples sintered under Ar with reference[56]

.

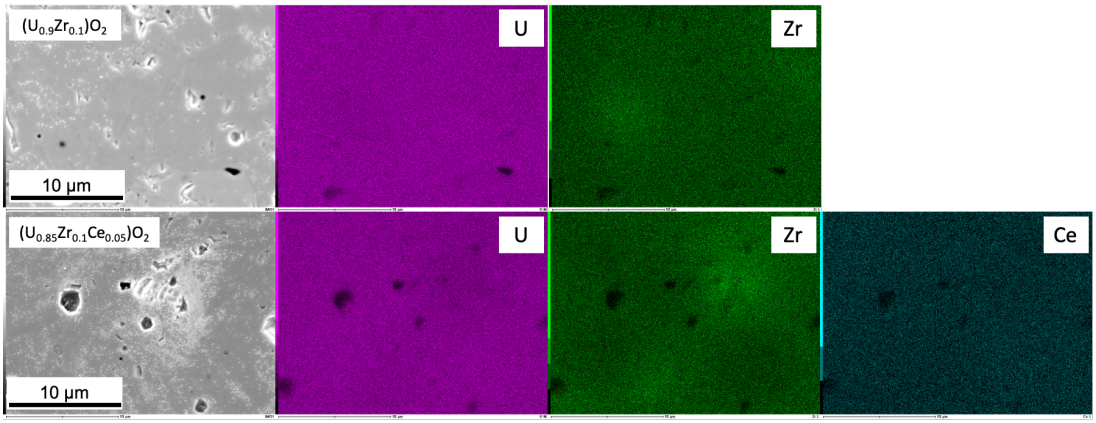

Figure 3 SEM/EDS images of the (U,Zr,Ce)O_2 samples sintered under Ar.

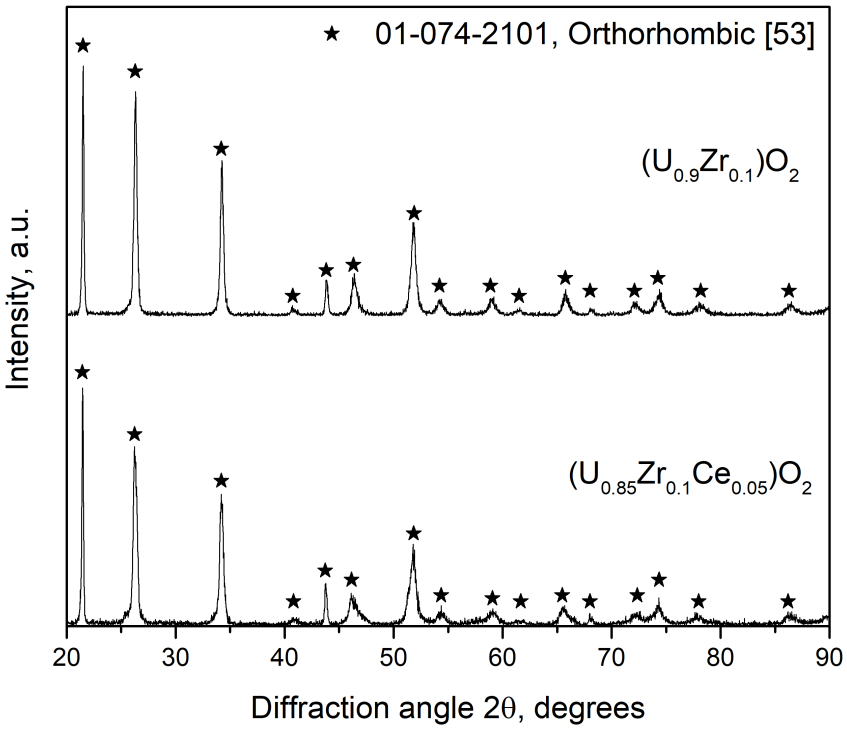

Figure 4 XRD patterns of the oxidized (U,Zr,Ce)O_2 samples with reference[51].

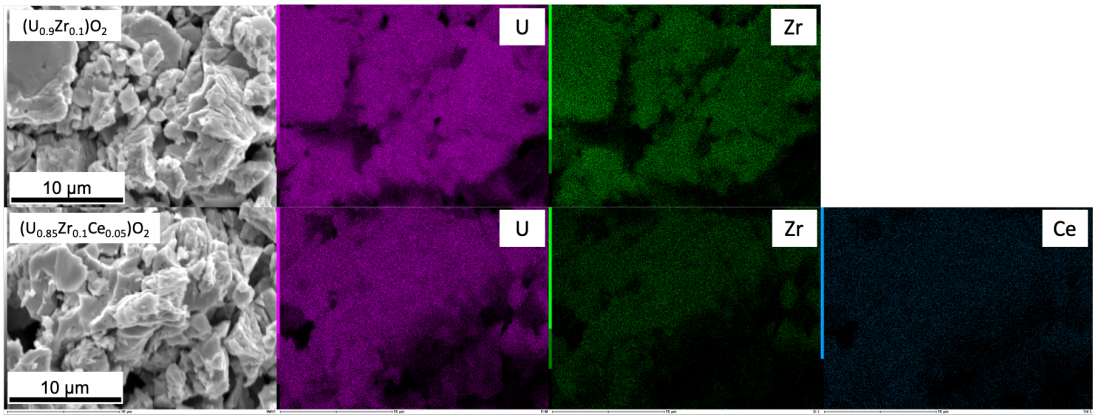

Figure 5 SEM/EDS images of the oxidized (U,Zr,Ce)O_2 samples

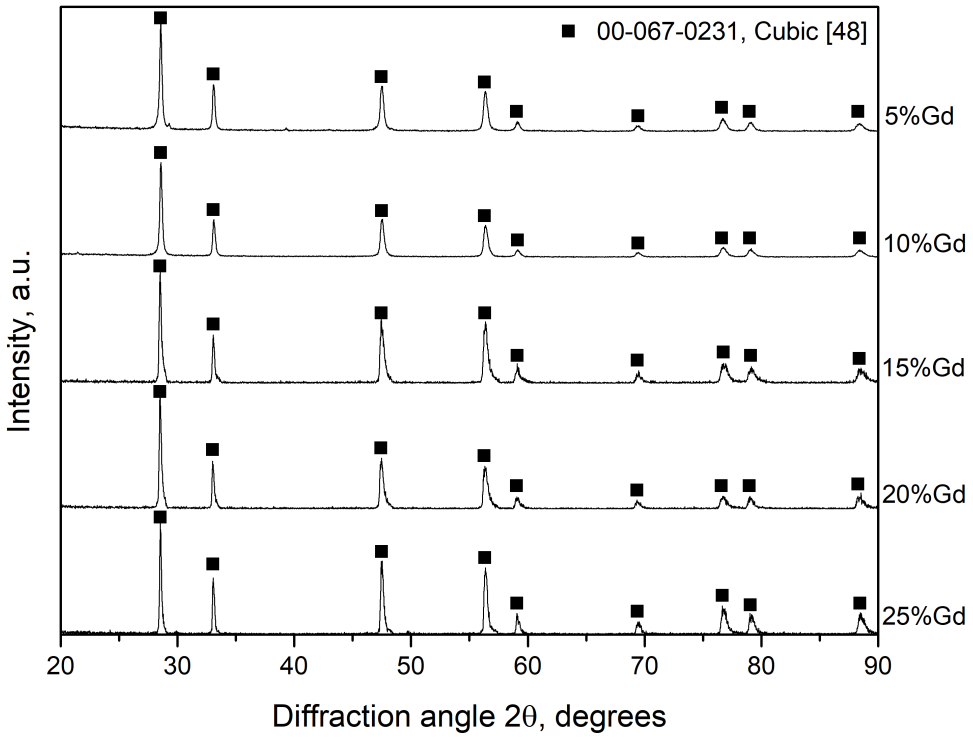

Figure 6 XRD patterns of the $(U_{1-x}Zr_{0.1}Gd_x)O_2$ samples sintered under Ar with reference[56]

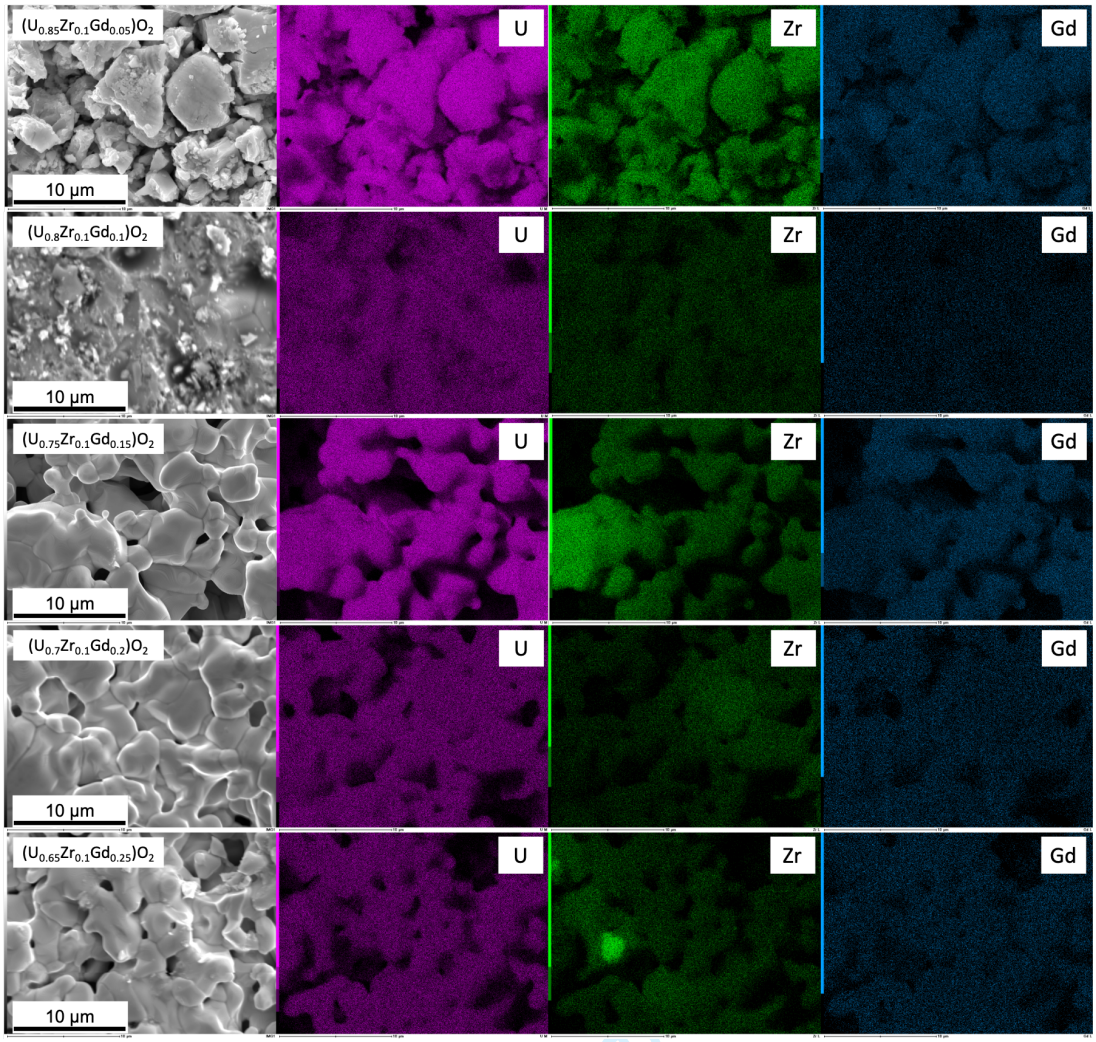

Figure 7 SEM/EDS images of the $(U_{1-x}Zr_{0.1}Gd_x)O_2$ samples sintered under Ar.

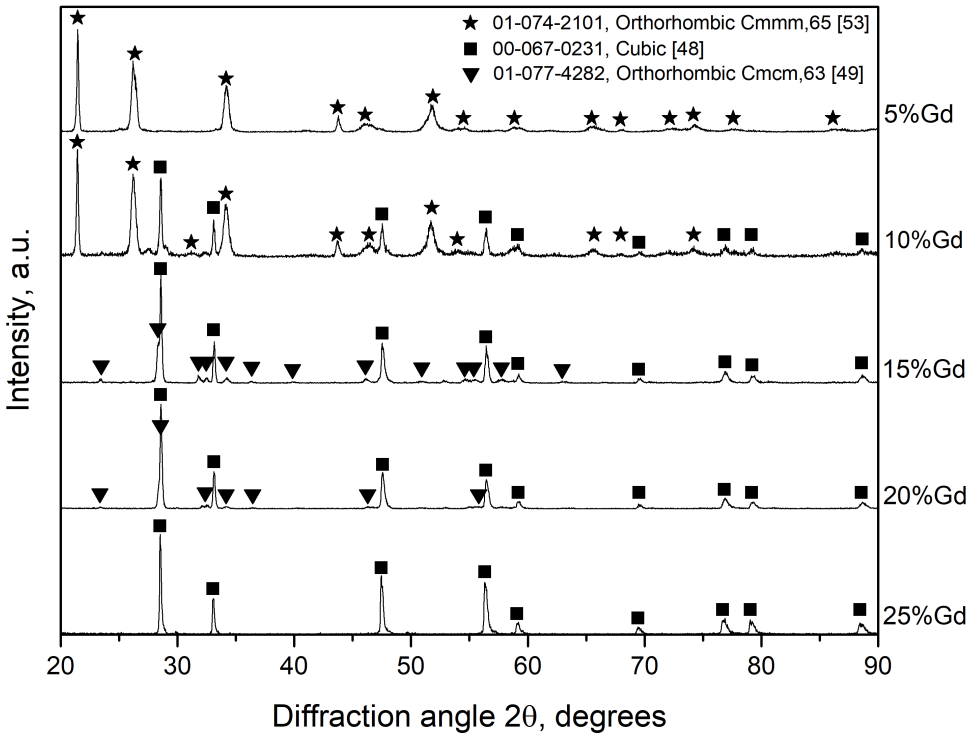

Figure 8 XRD patterns of the oxidized $(U_{1-x}Zr_{0.1}Gd_x)O_2$ samples with references[47, 51, 56].

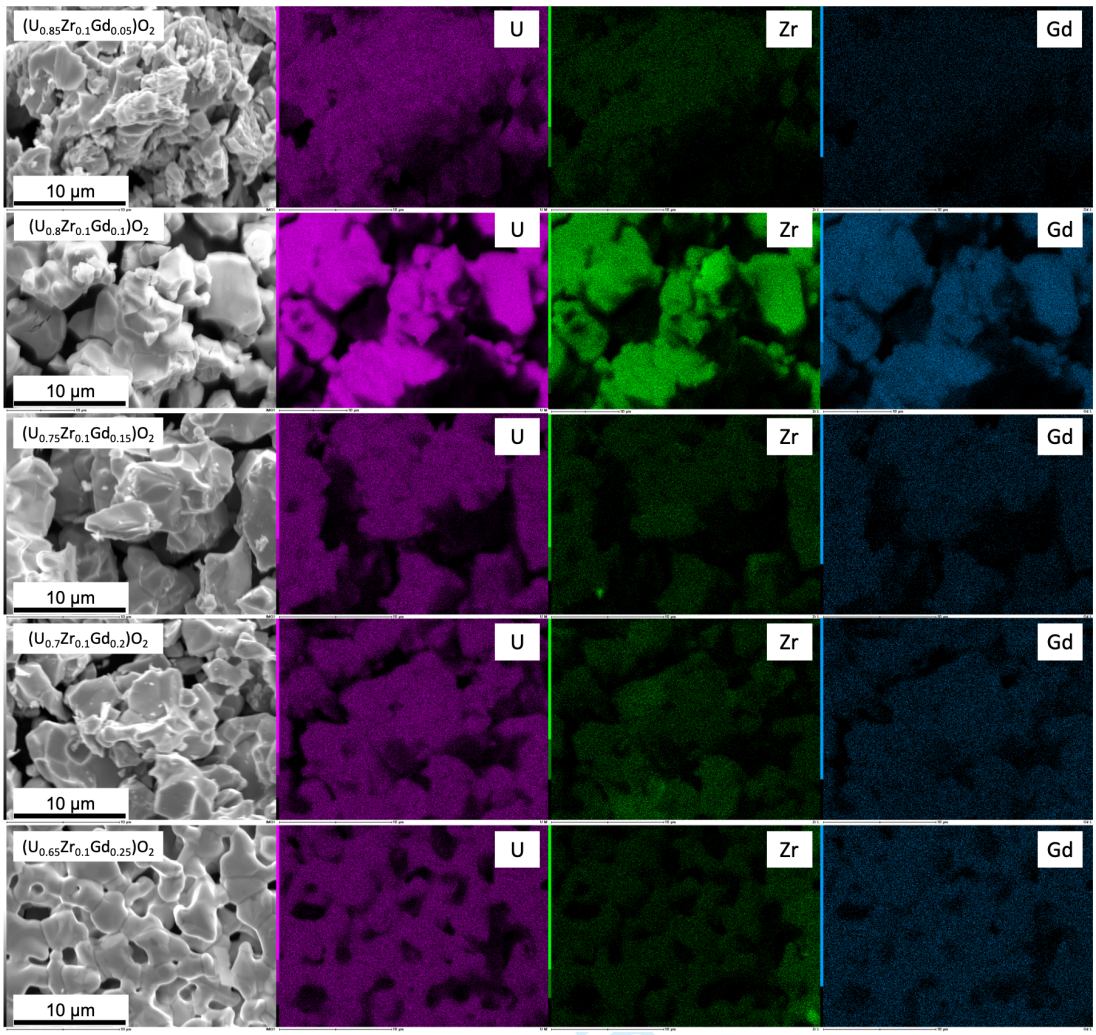

Figure 9 SEM/EDS images of the oxidized (U,Zr,Gd)O_2 samples